communications materials

A Nature Portfolio journal

Article

https://doi.org/10.1038/s43246-025-00809-z

Large trion binding energy in monolayer WS_2 via strain-enhanced electron–phonon coupling

Yunus Waheed[1,4], Sumitra Shit[1,4], Jithin T. Surendran[1], Indrajeet D. Prasad[1], Kenji Watanabe[2], Takashi Taniguchi[3] & Santosh Kumar[1]

Transition metal dichalcogenides and related layered materials in their monolayer and a few layers thicknesses regime provide a promising optoelectronic platform for exploring the excitonic- and many-body physics. Here, we have investigated the effects of nanoparticle-induced local strain on the optical properties of exciton, X^0, and trion, X^-, in monolayer WS_2. Biaxial tensile strain up to 2.0% was quantified and verified by monitoring the changes in three prominent Raman modes of WS_2: $E^1_{2g}(\Gamma)$, A_{1g}, and 2LA(M). We obtained an increase of 34 meV in X^- binding energy with an average tuning rate of 17.5 ± 2.5 meV/% strain across all the samples irrespective of the surrounding dielectric environment of monolayer WS_2 and the sample preparation conditions. Strain-induced linewidth broadening and deformation potentials of both X^0 and X^- emission elucidate that X^- binding energy increases due to strain-enhanced electron–phonon coupling. This work holds relevance for future X^--based nano-opto-electro-mechanical systems and devices.

Transition metal dichalcogenides (TMDs) are gaining significant interest in the scientific community due to possession of their unique optical and optoelectronic properties[1–3]. The properties on account of which TMDs stand out from other 2D material platforms are: indirect to direct bandgap conversion when they are thinned down to monolayer (ML) thicknesses[4–6], leading to stronger photoluminescence (PL) emission in visible and near-infrared spectral ranges[1,7], reduced dielectric screening resulting in enhanced Coulombic interactions in the ML regime gives rise to higher exciton binding energies, E_{b,X^0} (in the range of 0.2–1.0 eV)[8,9] and strong light–matter interactions[10]. TMDs have proven to be an ideal candidate for the next generation digital electronics due to their considerable bandgap[2]. Owing to their tunable bandgap, TMDs offer a platform for various electronic and opto-electronic applications[11]. To date, different methods, such as temperature, electric field, magnetic field, doping, and strain have been employed to effectively tune the electronic and optoelectronic properties of TMDs[12–14].

MLs of widely investigated TMDs, such as MoS_2, WS_2, $MoSe_2$, and WSe_2, show prominent emission peaks in their PL spectra that are red-shifted by 15–41 meV[9,15,16] from the ground-state (1s) neutral–excitonic, X^0, emission peaks. The formation of a singly-negative-charged trion, X^- due to intrinsic or substrate-related n-doping of the ML is the cause of such red-shifted peaks. The quasiparticle X^- presents a few observable advantages over X^0, such as its prolonged lifetime (by a factor of 5.0)[17], a higher degree (by a factor of 1.5) of valley polarization[18], and coupling to an additional electron. Upon dissociation of X^-, this system may allow us to control these fundamental charges' electronic spin, and valley properties. It is well established in the literature[19] that valley polarization plays a crucial role in valleytronic-based digital technology. The trion formation also enables the electrical control of exciton transport in TMD heterostructures, broadening their potential in various optoelectronic applications[20]. The energetic difference, $E_{b,X^-} = E_{X^0} - E_{X^-}$, where $E_{X^-}\left(E_{X^0}\right)$ is the emission energy of $X^-\left(X^0\right)$ transition, is referred to the X^- binding energy (BE)[3,21,22] or dissociation energy[23]. The values of E_{b,X^-} in ML-WS_2 falls in the range of 20–41 meV[3,15,23–25] owing to the nature of different dielectric environments. A lower E_{b,X^-} leads to thermal quenching due to lower thermal stability, resulting in the shortening of X^- lifetimes[26,27]. Thus, a requirement of increasing the E_{b,X^-} arise for efficiently controlling the X^-.

It has been demonstrated that the ramping up of excitation laser power results in an increase in $E_{b,,X^-}$ by a maximum of 5 meV[22,23,28]. Additionally, the use of laser light with high-order orbital angular momentum and at a higher excitation power has shown a substantial decrease of E_{b,X^-} by a maximum of 9 meV[22]. A limitation of this method is that the excitation power above a certain limit would lead to a local heating effect; hence, tuning over a wider range is not possible. Strain-tuning has emerged as a powerful

---

[1]School of Physical Sciences, Indian Institute of Technology Goa, Ponda, Goa, India. [2]Research Center for Electronic and Optical Materials, National Institute for Materials Science, Tsukuba, Japan. [3]Research Center for Materials Nanoarchitectonics, National Institute for Materials Science, Tsukuba, Japan. [4]These authors contributed equally: Yunus Waheed, Sumitra Shit. e-mail: skumar@iitgoa.ac.in

technique to tune the electronic properties and lattice dynamics of ML and a few-layer TMDs. An introduction of strain into the TMDs layers modifies the bandgaps and alters the effective masses and mobilities of charge carriers[29], leading to increased device performances. Uniaxial strain upto ≈2.2%[30] and biaxial strain up to ≈2.5%[31] have been introduced in 2D materials by bending the flexible substrates containing the flakes of 2D materials[25,30,32–36], by nano-indentation of 2D materials using sharp-tips like AFM-tip[37] and tapered fiber-tip[38], by pressurizing the cylindrical-cavity covered with the flakes[31], and by creating a thermal expansion coefficient mismatch between two materials[39,40]. Very recently, Henríquez-Guerra et al.[21], demonstrated the effects of biaxial strain on the E_{b,X^-} in ML-WS$_2$ and have shown an increase in E_{b,X^-} by ≈3 meV under the introduction of a 1.5% compressive strain.

Here, we have investigated the effects of local biaxial tensile-strain on PL emission properties of X^0 and X^- in ML-WS$_2$, and have demonstrated a significant increase in E_{b,X^-} by 34 meV and a five-fold enhancement in the emission intensity of X^-. We correlated the strain-induced broadening of both X^0 and X^- emission linewidths with their deformation potentials to conclude that the change in X^- BE is mainly governed by electron–phonon coupling mechanism. In this regard, we used a simple and cost-effective approach of imparting local strain on ML-WS$_2$ using spherical and shape-modified (see "Methods") dielectric (SiO$_2$) nanoparticles (NPs) as local stressors. The size distribution of NPs, together with the different levels of conformality of the flake at NP locations allowed us to explore strain in the range 0.1–2.0%. We performed micro-PL (μ-PL) spectroscopy to investigate excitonic emissions and micro-Raman (μ-Raman) spectroscopy for quantifying and verifying strain of strained ML-WS$_2$.

Results

Nanoparticle-induced local-strain effects on X^0 and X^- emission energies

We started our investigation with μ-PL measurements on Sample 1a. Figure 1a shows the PL peak intensity map of Sample 1a, displaying a strong light emission at all NP locations in the ML region of the flake due to a strain-induced funneling effect[41,42]. A one-to-one correlation of the strong light emission spots in the PL map with the dark contrast spots in the optical image can be seen in Supplementary Fig. S1. The deposition of a flake on top of the NPs-coated substrate has resulted in formations of different levels of conformalities: from a full conformality (see an SEM image in the left-inset of Fig. 1a to a tent-like structure (see an SEM image in the right-inset of Fig. 1a). The magnitude of local strain in the ML-WS$_2$ strongly depends on its extent of bending/conformality to the NPs and their size distribution, leading to a variation of local strain. This explicitly explains the different brightness of those NP-associated PL hotspots in Fig. 1a. Other features of the PL signal have also been affected greatly by this variation in the local strain.

In the next, we examine the effects of variation in local strain on emission energies of two important quasiparticles, X^0 and X^-, by acquiring PL spectra on all the NP locations as well as the unstrained regions in ML-WS$_2$. The statistical investigation of E_{X^0}, E_{X^-}, and E_{b,X^-} for both the strained and unstrained ML-WS$_2$ is presented in Fig. 1c in the form of Box-charts. Figure 1b compares a PL spectrum (open circles) taken at the NP16 location from the ML-WS$_2$ region, representing one of the highly strained conditions with another PL spectrum (closed circles) from the unstrained ML-WS$_2$. We employed a two-peak fitting function (solid lines), a Gaussian function for high-energy X^0 emission peak (dotted lines) and a Lorentzian function for low-energy X^- emission peak (dashed lines) for extracting the X^0 and X^- emission energies. On the unstrained region, we obtained an E_{b,X^-} of 32.3 meV which is well within the range (20–41 meV) of values reported in literature[3,15,23–25]. Narrower distributions of E_{X^0} and E_{X^-}, shown by solid boxes in the Box-charts are for unstrained ML-WS$_2$ and they indicate homogeneity of flake throughout the substrate. However, we observe wider distributions of E_{X^0} and E_{X^-} due to variation of strain at NP locations. On NP16, we observed a significant redshift of 36.8 meV in the E_{X^0} and a relatively large red-shift of 48.8 meV in E_{X^-} resulting a substantial increase in an E_{b,X^-} of 15.5 meV as shown in Fig. 1b. We obtain an average PL emission energy value of 2.008 eV (1.976 eV) (represented by small squares in solid Box-charts) corresponding to E_{X^0} (E_{X^-}) for the unstrained regions. As per literature, for unstrained ML-WS$_2$, the PL peak emission energies of X^0 and X^- at room temperature are 2.018 and 1.975 eV[43]. The values of X^0 and X^- emission energies in the unstrained region of Sample 1a are 2.009 and 1.976 eV. Due to the deposition of 75 nm-thick SiO$_2$ film with a lower dielectric constant than the 272 nm-thick thermally-grown SiO$_2$ layer on the Si-substrate, we observed a lower E_{X^0} in the unstrained region of ML-WS$_2$[44]. On the NP locations, an average emission energy value of 1.979 eV (1.935 eV) (represented by small squares in open Box-charts) corresponding to E_{X^0} (E_{X^-}) is observed. Analogous to the results on NP16, the average E_{b,X^-} for the unstrained flake comes out to be 32.5 meV while the average E_{b,X^-} from all measured NP locations is 44.3 meV, which is giving an average increased E_{b,X^-} of 11.8 meV as shown in the Fig. 1c. The red-shifts of E_{X^0} and E_{X^-} indicate toward the significant amount of local tensile strain created at the NP locations due to the bending of the flake[45].

Quantification of NP-induced local strain

For a quantitative understanding of local strain, we performed μ-Raman spectroscopy, in back-reflection geometry, on all investigated NP locations of ML-WS$_2$. Figure 2a shows a comparison of Raman spectra of ML-WS$_2$ taken on the NP16 location (open circles) with the Raman spectra taken at unstrained region (closed circles) in Sample 1a. We employed the Lorentzian peak fitting function to identify and extract the frequencies of all six different Raman modes in the Raman spectra of ML-WS$_2$ taken in the unstrained region and at the NP locations (see Supplementary Fig. S3). In accordance with our expectations, we observed different Raman shifts for all the six Raman modes of ML-WS$_2$ as shown by dotted vertical lines in Fig. 2a.

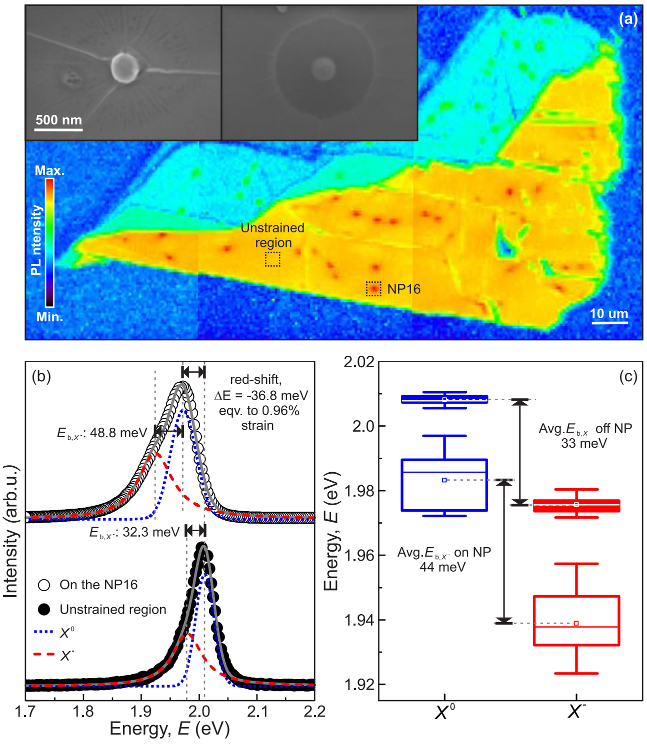

Fig. 1 | μ-PL and SEM characterization of Sample 1a. a Combined image of color-coded PL peak intensity maps of Sample 1a showing emission in the wavelength range of 535–880 nm. Inset: SEM images of two NPs with different flake conformalities: Conformality of flake according to the NP surface (left) and formation of tent-like structure on NP location. **b** Comparison of μ-PL spectra taken on-the-NP location (open circles, top) and unstrained region (closed circles, bottom) in ML-WS$_2$. Solid thick lines are the fits for the spectrum on-the-NP and unstrained locations. **c** Box-chart showing the X^0 and X^- emission energies distribution for unstrained and strained locations in the sample. Dotted gray lines show the distribution average for both strained and unstrained locations.

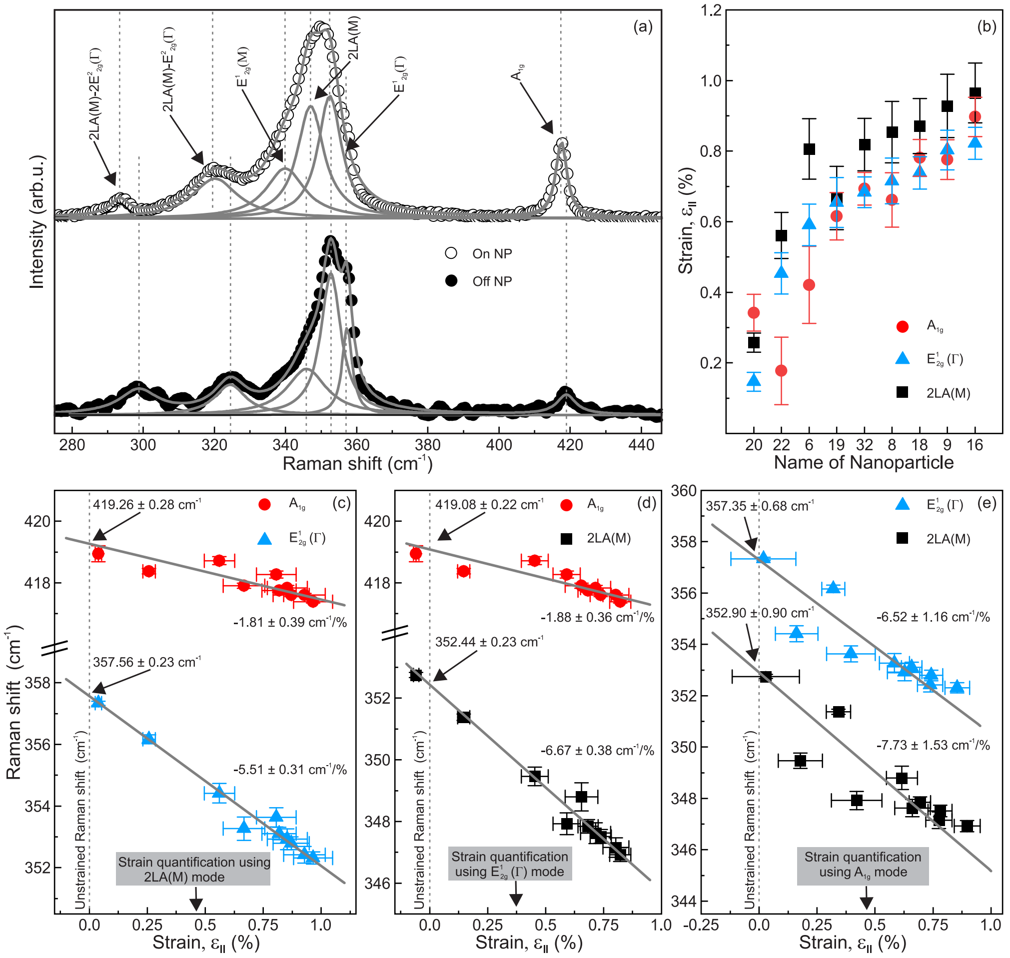

Fig. 2 | Strain quantification and its verification via different Raman modes in Sample 1a. a μ-Raman spectra taken on-the-NP location (open circles, top) and unstrained region (closed circles, bottom) of ML-WS_2. Solid thick lines are the fits for the spectrum on-the-NP and unstrained locations. **b** Plot showing the distribution of strain on different NP locations. **c** Raman shift of $E^1_{2g}(\Gamma)$ and A_{1g} modes as a function of strain quantified from 2LA(M) mode. **d** Raman shift of 2LA(M) and A_{1g} modes as a function of strain quantified from $E^1_{2g}(\Gamma)$ mode. **e** Raman shift of $E^1_{2g}(\Gamma)$ and 2LA(M) modes as a function of strain quantified from A_{1g} mode. The gray solid lines represent the linear fits. The error bars represent one standard deviation, considering measurement and fitting errors, and whichever is the higher.

We utilized three dominant and extensively studied Raman peaks: A_{1g}, $E^1_{2g}(\Gamma)$ and 2LA(M) in the Raman spectra of ML-WS_2 as three different probes to calculate strain created in the ML-WS_2 due to underneath NPs. As these three different peaks correspond to different modes of atomic vibrations in the crystal lattice, they exhibit different peak shifts in response to the particular magnitude of strain. We quantified the magnitude of local strain on multiple NP locations in Sample 1a, as shown in Fig. 2b using the shift rate of -1.8, -5.7, and -6.3 cm^{-1}/% strain and unstrained Raman shift frequencies of 419, 357, and 353 cm^{-1} for A_{1g}, $E^1_{2g}(\Gamma)$ and 2LA(M) modes of vibration[25,46]. As can be seen in Fig. 2b, the values of strain estimated using 2LA(M) and $E^1_{2g}(\Gamma)$ modes are within the error bar of each other showing agreement in the estimated values of strains. The distribution of NP sizes together with different levels of conformality of flake on the NP locations (see Supplementary Figs. S2 and S4) serve as local stress-inducing agents, enabling us to explore strain in the range of 0.1–1.0% in Sample 1a.

We further cross-verified the quantified strain through the following procedures. Figure 2c show the Raman shifts of $E^1_{2g}(\Gamma)$ and A_{1g} modes as a function of strain quantified from 2LA(M) mode. Similarly, Fig. 2d shows the Raman shifts of 2LA(M) and A_{1g} as a function of strain quantified from $E^1_{2g}(\Gamma)$ mode and Fig. 2e shows the Raman shifts of $E^1_{2g}(\Gamma)$ and 2LA(M) as a function of strain quantified from A_{1g} mode; the solid lines are the linear fits in all these three figures. It can be seen that the fitted values of Raman shifts of unstrained ML-WS_2 for all three Raman modes are in good agreement with the values reported in the literature (see also Supplementary Table S1). When we use 2LA(M) ($E^1_{2g}(\Gamma)$) mode to estimate the strain, then the verified shift-rates/% strain of the other two modes, $E^1_{2g}(\Gamma)$ and A_{1g} (2LA(M) and A_{1g}) are in agreement with the reference values that were utilized for strain estimation in the first hand. However, when the cross-verification of shift rates was done using the strain estimated from A_{1g}, the obtained shift rates/% strain of the other two modes showed considerable variations, although within the error bar. Thus, we observed that the strain estimation using A_{1g} mode underestimated the strain, and 2LA(M) and $E^1_{2g}(\Gamma)$ modes are the best methods for the strain estimation. The slight mismatch in the shift rate of A_{1g} peak from the reported shift rate can be attributed to the fact that A_{1g} is sensitive to doping concentration in the material[14,47].

Excitons' (X^0 and X^-) energy gauge-factors and X^- BE tuning rate

Post acquiring the strain from Raman modes, we correlated the E_{X^0} and E_{X^-} in PL spectra of ML-WS_2 with the measured strain in Sample 1a which is summarized in Fig. 3. The local strains plotted in Fig. 3a–c, have been quantified using A_{1g}, 2LA(M) and $E^1_{2g}(\Gamma)$ Raman modes, respectively. Taking into consideration that a small range of strains is accessed in this experiment, we performed linear fittings of these energy variations[15] and obtained values of $E^0_{X^0}$ $\left(E^0_{X^-}\right)$, emission energy of $X^0(X^-)$ transition in an unstrained ML-WS_2, that are plotted in Fig. 3d. From these fits (solid lines in Fig. 3), we also obtained $\Delta E_{X^0}/\%\left(\Delta E_{X^-}/\%\right)$ strain, an energy-gauge-factor of X^0 (X^-) transition in strained ML-WS_2, that are plotted in Fig. 3e. As can be seen in Fig. 3d, we obtained slightly different values of E_{X^0} and

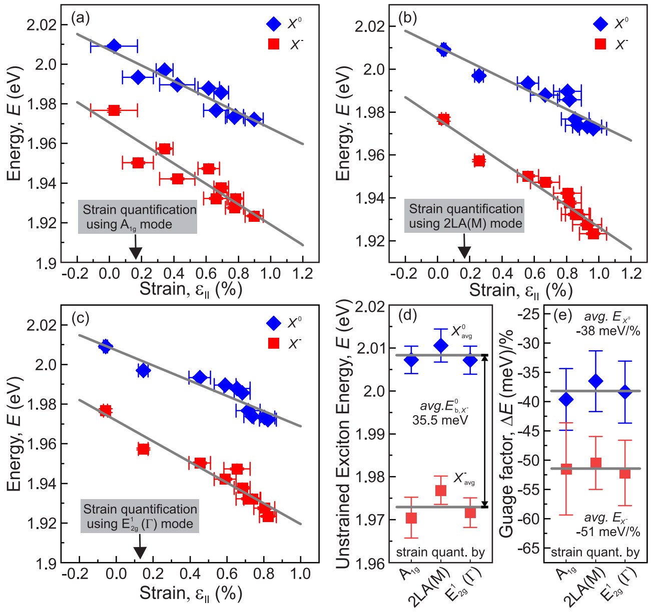

Fig. 3 | Binding-energy tuning-rate per % biaxial strain (gauge factor) of X^- emission in ML-WS$_2$ in Sample 1a. X^0 and X^- emission energies as a function of strain quantified using (**a**) A$_{1g}$, (**b**) 2LA(M) and (**c**) E$^1_{2g}$(Γ) Raman modes, showing unequal energy tuning rates leading to a change in the binding energy of X^-. **d** X^0 and X^- emission energies of unstrained ML-WS$_2$ and **e** X^0 and X^- energy gauge factors of ML-WS$_2$ quantified using A$_{1g}$, 2LA(M) and E$^1_{2g}$(Γ) Raman modes. The diamonds and squares are for X^0 and X^-, respectively. The solid lines in (**a–c**) represent the linear fits and in (**d**) and (**e**) represent the averages. The error bars represent one standard deviation, considering measurement and fitting errors, and whichever is the higher.

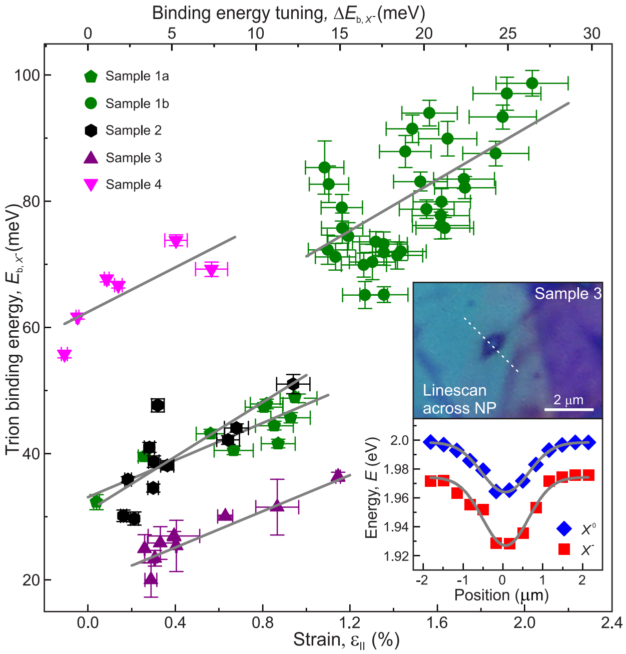

Fig. 4 | Strain tuning-rate of trion's binding energy, $\Delta E_{b,X^-}$/% across various samples. Strain-dependent trion's binding energy, E_{b,X^-} for Sample 1a (pentagons), Sample 1b (circles), Sample 2 (hexagons), Sample 3 (triangles) and Sample 4 (inverted triangles), showing a very similar tuning-rates of trion binding energy per % of biaxial strain. Inset: The optical micrograph of Sample 3. A dotted line is representing the PL linescan (top) and the change in X^0 (diamonds) and X^- (squares) PL peak energy positions as a function of distance across the NP location (bottom). The error bars represent one standard deviation, considering measurement and fitting errors, and whichever is the higher.

E_{X^-} for unstrained ML-WS$_2$ using different strain estimating Raman modes. The average (solid line) of these three $E_{X^0}(E_{X^-})$ values is 2.008 (1.973) eV, which is similar to the value obtained in the statistical PL investigation of unstrained ML-WS$_2$. Similarly, we obtained the average $\Delta E_{X^0}/\%(\Delta E_{X^-}/\%)$ strain of -38 ± 3.0 (-51 ± 3.5) meV/% strain for emission energies of X^0 (X^-) transition, which are well within the range of −11 to −130 meV/% strain, reported in the literature[13,25]. Both uniaxial and biaxial strains have been utilized to estimate the gauge factors of X^0 and X^- in ML TMDs, as summarized in Supplementary Table S2. However, the strain introduction methods primarily rely on the method of substrate bending in a two-point (four-point) configuration, resulting in uniaxial (biaxial) strain throughout the flake. The use of NPs as stress inducers facilitates the introduction of localized strain right at the NP's location. This approach allows for the precise introduction of strain in the region of interest, minimizing the need for global substrate deformation. As the emission of light due to X^- happens at a lower energy than X^0, the difference in X^0 and X^- gauge factors lead to an increase in the BE of X^- with a tuning rate, $\Delta E_{b,X^-}$/%, of 13 ± 4.5 meV/% strain for Sample 1a.

We attribute this significant change in E_{b,X^-} to the pronounced variation in the local strain that can be qualitatively understood in terms of strain-induced variations in the interaction energies between the constituent particles of X^0 and X^- in ML-WS$_2$. The quasiparticle X^- consists of two electrons (e^-) and one hole (h), and the interaction energies between these constituent particles play a significant role in contributing to the E_{b,X^-} of ML-WS$_2$. Biaxial strain induces changes in both electron-hole interaction energy (J_{eh}) as well as electron–electron interaction energy (J_{ee}). However, for a strongly 2D-confined system, under the assumption that strain induces negligible changes in the single-particle confinement energies, the rate of change of E_{b,X^-} per unit strain is given by:

$$\frac{d}{d\epsilon_{\parallel}}\left(E_{b,X^-}\right) \approx \frac{d}{d\epsilon_{\parallel}}\left(J_{eh}\right) - \frac{d}{d\epsilon_{\parallel}}\left(J_{ee}\right) \quad (1)$$

Ding et al.[48], have shown that with increasing biaxial tensile strain, the decrease in the second term in Eq. (1) is more significant as compared to the first term, therefore rendering a positive value of dE_{b,X^-}/d$\epsilon_{\parallel}$. It clearly indicates the increase in X^- BE for ML-WS$_2$ via the introduction of biaxial tensile strain.

X^- tuning-rates verification across various samples

To authenticate this large tuning rate, $\Delta E_{b,X^-}$/%, we investigated four more samples with optically active material ML-WS$_2$ and findings are summarized in Fig. 4. It is expected that strain will decrease as we move away from the center of NPs. Therefore, in Sample 3, a single and isolated NP location was investigated by performing a line-scan PL measurement. The optical micrograph of the Sample 3 showing the isolated NP location and changes in the X^0 and X^- energies are shown in the inset of Fig. 4. We utilized a gauge factor ΔE_{X^0}/% biaxial strain, −38 meV/% that is obtained in Sample 1a, to estimate strain in all the samples. Figure 4 shows the variation of E_{b,X^-} as a function of strain for all investigated samples where the pentagons, circles, hexagons, triangles and inverted triangles represent the measured data points for Samples 1a, 1b, 2, 3, and 4, respectively. $\Delta E_{b,X^-}$/% biaxial strain obtained from the linear fitting of measured data from all five samples are summarized in Table 1, and it shows that $\Delta E_{b,X^-}$/% biaxial strain for all samples are similar and within the error bars. Conclusively, we state that on average, we obtain the tuning rate of X^- BE, $\Delta E_{b,X^-}$/% biaxial strain of 17.5 ± 2.5 meV/%.

Correlation of enhanced X^- BE with electron–phonon coupling

Looking at the fact that the local strain has increased the energetic separation between X^0 and X^- transitions, it is expected to alter the transition probability of both transitions. In the following, we inspect this aspect by monitoring the emission intensity and linewidth of both the transitions, and the outcome is summarized in Fig. 5. Figure 5a shows the I_{X^-}/I_{X^0} ratios for all the investigated samples, where I_{X^0} (I_{X^-}) is the intensity of X^0(X^-) that are plotted as a function of strain. In each investigated sample, we noticed a clear increase in the I_{X^-}/I_{X^0} ratio with increasing strain. Along with the increase in the I_{X^-}/I_{X^0}, we observed two different sets of data points. Although both the data sets show a similar increase in the intensity ratio I_{X^-}/I_{X^0}, the minimum intensity ratio of one data set is higher than the other because of different dielectric environment and sample preparation conditions. However, irrespective of the value of strain quantified for different samples, we observed up to ≈5 × enhancement in the I_{X^-}/I_{X^0} ratio on the introduction of up to 2% tensile strain. This observation is in accordance with the mass action law exhibiting an increase in the I_{X^-}/I_{X^0} with increasing E_{b,X^-} that is increasing with strain[16,22]. Also, we monitored the strain-induced broadening (increase) in the full width at half maximum, linewidth, of X^0 and X^- emission peaks for all investigated samples, which is summarized in Fig. 5. As per literature, the broadening in the linewidth of excitonic emission peak in the PL spectra as a function of strain has only been observed for MoS_2 with a broadening rate of 10–15 meV/%[49,50] while $MoSe_2$, WS_2, and WSe_2 showed narrowing (decrease) in linewidth as function of strain with rates 5, 8, and 20 meV/%, respectively[50]. Our linewidth vs strain data for both X^0 and X^- peaks of ML-WS_2 plotted in Fig. 5b, c show a clear broadening in the linewidth under tensile strain. The linear fits of the measured data produced a linewidth shift rate of 42 meV/% (71 meV/%) biaxial strain for X^0(X^-) which shows that the phonon is interacting more strongly with X^- than X^0. Shen et al.[51] have shown that the valence bands of WSe_2 are not much affected by strain up to 2%. Thus, we further investigated these strain effects on excitons through the coupling strength of electron–phonon interaction that is given by:

$$\beta \propto \frac{DP^2}{Y} \tag{2}$$

where, DP is the gap deformation potential of the quasiparticle, and Y is Young's Modulus of elasticity. In this work, since we are monitoring the $\Delta E_{X^0(X^-)}$, we can calculate the DP of both the transitions given by[52]:

$$DP_{X^0(X^-)} = \frac{\Delta E_{X^0(X^-)}}{(2-\rho)\cdot\epsilon_\parallel} \tag{3}$$

where, ρ (= 0.19) is the Poisson's ratio of ML-WS_2, $\epsilon_\parallel$ refers to local strain, which we have also measured in this work. Since, $\Delta E_{X^0(X^-)}$ per unit strain can be obtained from Fig. 3, the calculated $DP_{X^0(X^-)}$ is 2.10 (2.82) eV, giving rise to coupling strengths ratio of electron–phonon interaction for X^0 and X^-, $\beta_{X^-}/\beta_{X^0} = 1.80 \pm 0.27$. It is striking to see that aforementioned ratio of coupling strengths of electron–phonon interaction for X^0 and X^-, which is obtained from the strain-induced energy changes in them, also agrees well with the ratio of linewidth shift rates of X^0 and X^-, $\Delta\omega_{X^-}/\Delta\omega_{X^0}$ per percent strain, rendering a value of 1.71 ± 0.14. From this, we conclude that the strain-induced changes in the binding energies of X^- can be explained by electron–phonon interactions. A further understanding of electron–phonon coupling at a length scale less than the optical diffraction limit can be developed by investigating the optical signals at a few nanometer length scales, e.g., by using the scanning near-field optical microscopy technique.

Table 1 | X^- BE tuning-rate per % biaxial strain (gauge factor) of ML-WS_2 for all samples

Sample	Tuning-rate of trion's BE, $\Delta E_{b,X^-}$/% biaxial strain meV/%
Sample 1a	13.0 ± 4.5
Sample 1b	20.0 ± 5.0
Sample 2	21.5 ± 5.5
Sample 3	14.5 ± 2.5
Sample 4	17.5 ± 7.0

Discussion

In this work, we report the large increase of X^- BE by 34 meV due to strain-enhanced electron–phonon coupling in ML-WS_2. To demonstrate this

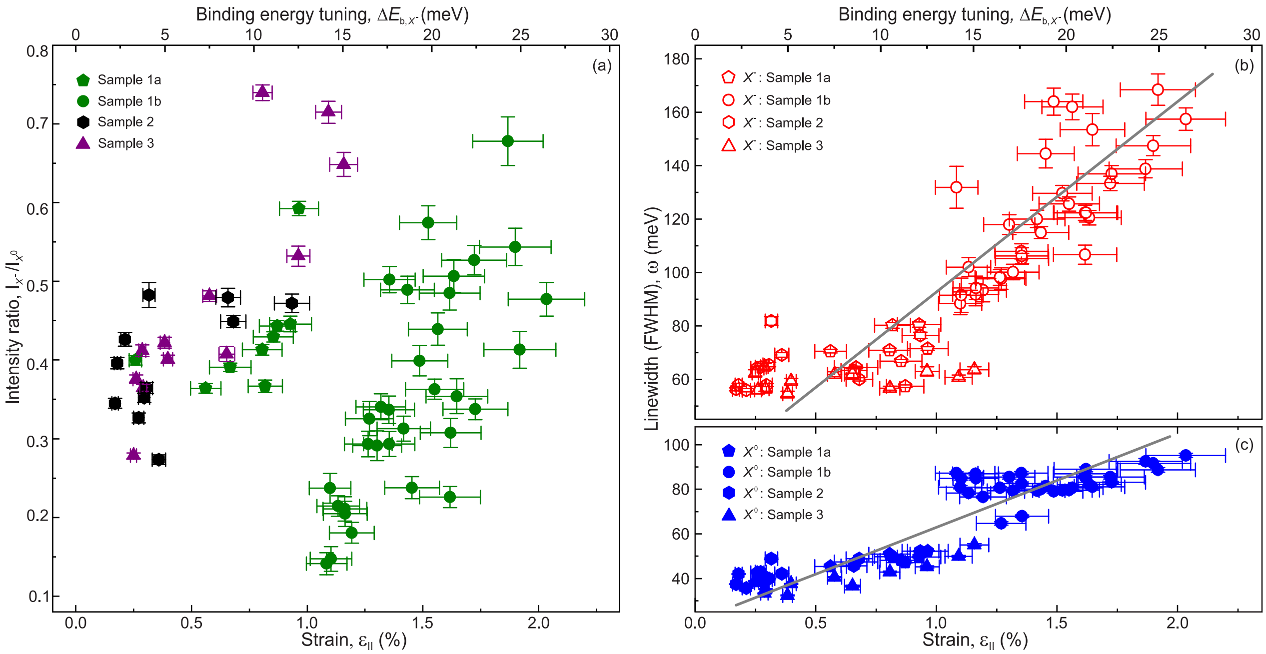

Fig. 5 | Strain-dependent PL emission intensity and linewidth (FWHM) of X^0 and X^- emission across different samples. **a** Strain-dependent ratio of the intensity of X^- emission peak (I_{X^-}) to the intensity of X^0 emission peak for Sample 1a (pentagons), Sample 1b (circles), Sample 2 (hexagons) and Sample 3 (triangles). Strain-dependent linewidth of **b** X^- and **c** X^0 emission peaks, for all the investigated samples. Pentagons, circles, hexagons and triangles in (**b**) and (**c**) are for Samples 1a, 1b, and 3, respectively. The error bars represent one standard deviation, considering measurement and fitting errors, and whichever is the higher.

strain-induced variation, we investigated the emission energies of X^0 and X^- by performing the μ-PL measurements on unstrained and NP locations in ML-WS$_2$ across different samples. The strain in ML-WS$_2$ was quantified by performing the Raman measurements as described in Fig. 2a, b. Three dominant and extensively studied Raman modes: A$_{1g}$, E$^1_{2g}$(Γ), and 2LA(M) modes were employed for this strain quantification. The cross-verification of strain was done by plotting the Raman shift frequencies of two Raman modes against the strain quantified from the third Raman mode. This process was utilized for all three Raman modes as described in Fig. 2. We further correlated the strain-induced variations in the peak emission energies of X^0 and X^- transitions of ML-WS$_2$ with the quantified strain as summarized in Fig. 3 and obtained the energy gauge factor of $X^0(X^-)$, $\Delta E_{X^0}/\%\left(\Delta E_{X^-}/\%\right)$ strain, of −38 ± 3.0 (−51 ± 3.5) meV/% biaxial strain leading to X^- BE tuning rate, $\Delta E_{b,X^-}/\%$ strain, of 13 ± 4.5 meV/% strain, as shown in Fig. 3e. To further verify this strain-induced large tuning rate, we investigated the PL spectra of strained ML-WS$_2$ from four additional samples as shown in Fig. 4, where the strain was quantified using the gauge factor of −38 meV/% biaxial strain obtained from Sample 1a. The distribution in sizes of NPs and different levels of conformality of the flake on NP locations enabled us to explore strain in the range 0.1–2.0% across all samples. Utilizing the excitonic gauge factor, where strain was quantified via Raman spectroscopy of Sample 1a, we achieved similar X^- BE tuning rates for other four samples, highlighting the consistency of this approach. Conclusively, we obtained an average $\Delta E_{b,X^-}/\%$ strain of 17.5 ± 2.5 meV/% for all the investigated samples irrespective of the surrounding dielectric environment of ML-WS$_2$ and the sample preparation conditions summarized in Table 1 and we have shown that this large change in BE can be understood in terms of the interaction energies between the constituent particles in X^0 and X^- quasiparticles. Alongside the large variation in X^- BE, we also investigated the strain-induced linewidth broadening shown in Fig. 5b, c and the deformation potentials of both the X^0 and X^- transitions and hence, elucidated the significant role of strain-enhanced electron–phonon coupling in increasing the X^- BE. We believe that the technique utilized in this work can be employed to enhance electron–phonon interactions via localized strain in other TMDs and their exotic heterostructures[53–55] to tune the optical properties of excitons and trions at room temperature. This strain-induced increase in the E_{b,X^-} followed by enhanced stability and efficient formation of X^- holds relevance for future X^- based nano-opto-electro-mechanical systems even at elevated temperatures.

Methods

Sample preparation

The studied samples consist of three different layered structures. Samples 1 and 4 (Sample 2) consist of mechanically exfoliated ML-WS$_2$ deposited on shape-modified (spherical) SiO$_2$-NPs distributed over a SiO$_2$ (272 nm)/Si substrate. Utilizing the spin-coating method, we obtained a random distribution of individual NPs that are well isolated from each others on all samples. The size of spherical NPs (Sigma-Aldrich) falls typically in the range of 125–175 nm. These NPs act as nano stressors, creating local strain in ML-WS$_2$. NP concentration in ethanol was optimized to prevent agglomeration. In Samples 1 and 4, the process of shape modification of NPs was accomplished through deposition of 75 nm-thick SiO$_2$ film on spherical-NPs distributed over a SiO$_2$/Si substrate using an e-beam physical vapor deposition technique. The active material, ML-WS$_2$, is then deposited on top of shape-modified-NPs. In Sample 3, NPs were spin-coated onto the bottom-hBN deposited on SiO$_2$/Si substrate, followed by transfer of ML-WS$_2$, which is further encapsulated by a thin-hBN flake. Both the WS$_2$ and hBN flakes were mechanically exfoliated from their bulk counterparts. The ML-WS$_2$ flakes were qualitatively identified by optical color contrast and further confirmed by PL and Raman spectroscopy. We employed the conventional dry-transfer method using polydimethylsiloxane stamps to transfer the flakes on top of each other[56]. We also noticed wrinkles formation during the top-thin hBN transfer because of the high elastic modulus of the hBN[57] compared to ML-WS$_2$[58]. As a standard protocol of sample processing, we employed vacuum annealing at 200 °C for 5 h, followed by natural cooling in a rapid-thermal-annealing system for Samples 1 and 3[59].

PL and Raman spectroscopy

PL and Raman signals from all three samples were collected using a home-built confocal microscopy setup equipped with a microscope objective (NA = 0.75), yielding diffraction-limited spatial resolutions. The samples were mounted on an XY scanner combined with a ±2.5 mm XYZ nano-positioner stack (Attocube). For generating the space maps of PL signals, the samples were moved using the scanner providing a scanning range of 50 μm. A diode-pumped solid-state CW laser emitting at λ = 532 nm was used as an exciting source for both PL and Raman measurements. An ultra-steep long pass filter designed at an edge of 533.3 nm (Semrock) was used to suppress the laser light from entering into the spectrometer. All the spectra were acquired with a 0.5 m focal length spectrometer combined with a water-cooled charge-coupled device camera providing a best spectral resolution of ~125 μeV at λ = 532 nm on an 1800 lines/mm grating. A grating with 150 lines/mm giving a spectral resolution of 2.5 meV at λ = 532 nm was used for acquiring large wavelength range spectra.

Data availability

The data that support the findings of this study are available from the corresponding author upon reasonable request.

Received: 21 November 2024; Accepted: 17 April 2025;

References

1. Mak, K. F., Lee, C., Hone, J., Shan, J. & Heinz, T. F. Atomically thin MoS$_2$: a new direct-gap semiconductor. *Phys. Rev. Lett.* **105**, 136805 (2010).
2. Butler, S. Z. et al. Progress, challenges, and opportunities in two-dimensional materials beyond graphene. *ACS Nano* **7**, 2898 (2013).
3. Mak, K. F. et al. Tightly bound trions in monolayer MoS$_2$. *Nat. Mater.* **12**, 207 (2013).
4. Manzeli, S., Ovchinnikov, D., Pasquier, D., Yazyev, O. V. & Kis, A. 2D transition metal dichalcogenides. *Nat. Rev. Mater.* **2**, 1 (2017).
5. Chhowalla, M. et al. The chemistry of two-dimensional layered transition metal dichalcogenide nanosheets. *Nat. Chem.* **5**, 263 (2013).
6. Zheng, W. et al. Light emission properties of 2D transition metal dichalcogenides: fundamentals and applications. *Adv. Opt. Mater.* **6**, 1800420 (2018).
7. Splendiani, A. et al. Emerging photoluminescence in monolayer MoS$_2$. *Nano Lett.* **10**, 1271 (2010).
8. Mueller, T. & Malic, E. Exciton physics and device application of two-dimensional transition metal dichalcogenide semiconductors. *npj 2D Mater. Appl* **2**, 29 (2018).
9. Zhu, B., Chen, X. & Cui, X. Exciton binding energy of monolayer WS$_2$. *Sci. Rep.* **5**, 9218 (2015).
10. Wurstbauer, U., Miller, B., Parzinger, E. & Holleitner, A. W. Light–matter interaction in transition metal dichalcogenides and their heterostructures. *J. Phys. D Appl. Phys.* **50**, 173001 (2017).
11. Wang, Q. H., Kalantar-Zadeh, K., Kis, A., Coleman, J. N. & Strano, M. S. Electronics and optoelectronics of two-dimensional transition metal dichalcogenides. *Nat. Nanotechnol.* **7**, 699 (2012).
12. Mas-Balleste, R., Gomez-Navarro, C., Gomez-Herrero, J. & Zamora, F. 2D materials: to graphene and beyond. *Nanoscale* **3**, 20 (2011).
13. Wang, Y. et al. Strain-induced direct–indirect bandgap transition and phonon modulation in monolayer WS$_2$. *Nano Res.* **8**, 2562 (2015).
14. Sasaki, S. et al. Growth and optical properties of Nb-doped WS$_2$ monolayers. *Appl. Phys. Express* **9**, 071201 (2016).
15. He, X. et al. Strain engineering in monolayer WS$_2$, MoS$_2$, and the WS$_2$/MoS$_2$ heterostructure. *Appl. Phys. Lett.* **109**, 173105 (2016).
16. Dastidar, M. G. et al. Optically induced trion formation and its control in MoS$_2$/graphene van der waals heterostructure. *Nanoscale* **16**, 19413 (2024).

17. Wang, G. et al. Valley dynamics probed through charged and neutral exciton emission in monolayer WSe_2. *Phys. Rev. B* **90**, 075413 (2014).
18. Hao, K. et al. Trion valley coherence in monolayer semiconductors. *2D Mater.* **4**, 025105 (2017).
19. Schaibley, J. R. et al. Valleytronics in 2D materials. *Nat. Rev. Mater.* **1**, 1 (2016).
20. Bellus, M. Z., Ceballos, F., Chiu, H.-Y. & Zhao, H. Tightly bound trions in transition metal dichalcogenide heterostructures. *ACS Nano* **9**, 6459 (2015).
21. Henríquez-Guerra, E. et al. Large biaxial compressive strain tuning of neutral and charged excitons in single-layer transition metal dichalcogenides. *ACS Appl. Mater. Interfaces* **15**, 57369 (2023).
22. Kesarwani, R. et al. Control of trion-to-exciton conversion in monolayer WS_2 by orbital angular momentum of light. *Sci. Adv.* **8**, eabm0100 (2022).
23. Mitioglu, A. et al. Optical manipulation of the exciton charge state in single-layer tungsten disulfide. *Phys. Rev. B Condens. Matter Mater. Phys.* **88**, 245403 (2013).
24. Ross, J. S. et al. Electrical control of neutral and charged excitons in a monolayer semiconductor. *Nat. Commun.* **4**, 1474 (2013).
25. Michail, A. et al. Tuning the photoluminescence and Raman response of single-layer WS_2 crystals using biaxial strain. *J. Phys. Chem. C* **127**, 3506 (2023).
26. Golovynskyi, S. et al. Trion binding energy variation on photoluminescence excitation energy and power during direct to indirect bandgap crossover in monolayer and few-layer MoS_2. *J. Phys. Chem.* **125**, 17806 (2021).
27. Golovynskyi, S. et al. Exciton and trion in few-layer MoS_2: thickness- and temperature-dependent photoluminescence. *Appl. Surf. Sci.* **515**, 146033 (2020).
28. Chowdhury, T. et al. Modulation of trion and exciton formation in monolayer WS_2 by dielectric and substrate engineering. *2D Mater.* **8**, 045032 (2021).
29. Amin, B., Kaloni, T. P. & Schwingenschlögl, U. Strain engineering of WS_2, WSe_2, and WTe_2. *RSC Adv.* **4**, 34561 (2014).
30. Conley, H. J. et al. Bandgap engineering of strained monolayer and bilayer MoS_2. *Nano Lett.* **13**, 3626 (2013).
31. Lloyd, D. et al. Band gap engineering with ultralarge biaxial strains in suspended monolayer MoS_2. *Nano Lett.* **16**, 5836 (2016).
32. Chang, H.-Y. et al. High-performance, highly bendable MoS_2 transistors with high-k dielectrics for flexible low-power systems. *ACS Nano* **7**, 5446 (2013).
33. Park, S. et al. Transparent nanoscale polyimide gate dielectric for highly flexible electronics. *Adv. Electron. Mater.* **4**, 1700043 (2018).
34. Carrascoso, F., Frisenda, R. & Castellanos-Gomez, A. Biaxial versus uniaxial strain tuning of single-layer MoS_2. *Nano Mater. Sci.* **4**, 44 (2022).
35. Carrascoso, F. et al. Improved strain engineering of 2D materials by adamantane plasma polymer encapsulation. *npj 2D Mater. Appl*. **7**, 24 (2023).
36. Michail, A. et al. Biaxial strain engineering of CVD and exfoliated single-and bi-layer MoS_2 crystals. *2D Mater.* **8**, 015023 (2020).
37. Harats, M. G., Kirchhof, J. N., Qiao, M., Greben, K. & Bolotin, K. I. Dynamics and efficient conversion of excitons to trions in non-uniformly strained monolayer WS_2. *Nat. Photon.* **14**, 324 (2020).
38. Gelly, R. J. et al. Probing dark exciton navigation through a local strain landscape in a WSe_2 monolayer. *Nat. Commun.* **13**, 232 (2022).
39. Frisenda, R. et al. Biaxial strain tuning of the optical properties of single-layer transition metal dichalcogenides. *npj 2D Mater. Appl.* **1**, 10 (2017).
40. Plechinger, G. et al. Control of biaxial strain in single-layer molybdenite using local thermal expansion of the substrate. *2D Mater.* **2**, 015006 (2015).
41. Moon, H. et al. Dynamic exciton funneling by local strain control in a monolayer semiconductor. *Nano Lett.* **20**, 6791 (2020).
42. Branny, A., Kumar, S., Proux, R. & Gerardot, B. D. Deterministic strain-induced arrays of quantum emitters in a two-dimensional semiconductor. *Nat. Commun.* **8**, 15053 (2017).
43. Plechinger, G. et al. Identification of excitons, trions and biexcitons in single-layer WS_2. *Phys. Stat. Sol. RRL* **9**, 457 (2015).
44. Hsu, W.-T. et al. Dielectric impact on exciton binding energy and quasiparticle bandgap in monolayer WS_2 and WSe_2. *2D Mater.* **6**, 025028 (2019).
45. Castellanos-Gomez, A. et al. Local strain engineering in atomically thin MoS_2. *Nano Lett.* **13**, 5361 (2013).
46. Zhang, X. et al. Phonon and Raman scattering of two-dimensional transition metal dichalcogenides from monolayer, multilayer to bulk material. *Chem. Soc. Rev.* **44**, 2757 (2015).
47. Dhakal, K. P. et al. Confocal absorption spectral imaging of MoS_2: optical transitions depending on the atomic thickness of intrinsic and chemically doped MoS_2. *Nanoscale* **6**, 13028 (2014).
48. Ding, F. et al. Tuning the exciton binding energies in single self-assembled InGaAs/GaAs quantum dots by piezoelectric-induced biaxial stress. *Phys. Rev. Lett.* **104**, 067405 (2010).
49. Niehues, I. et al. Strain control of exciton–phonon coupling in atomically thin semiconductors. *Nano Lett.* **18**, 1751 (2018).
50. Khatibi, Z. et al. Impact of strain on the excitonic linewidth in transition metal dichalcogenides. *2D Mater.* **6**, 015015 (2018).
51. Shen, T., Penumatcha, A. V. & Appenzeller, J. Strain engineering for transition metal dichalcogenides based field effect transistors. *ACS Nano* **10**, 4712 (2016).
52. Prasad, I. D.et al. Measurements of absolute bandgap deformation-potentials of optically-bright bilayer WSe_2, arXiv:2412.00453 (2024).
53. Sun, X. et al. Enhanced interactions of interlayer excitons in free-standing heterobilayers. *Nature* **610**, 478 (2022).
54. Montblanch, A. R.-P. et al. Confinement of long-lived interlayer excitons in WS_2/WSe_2 heterostructures. *Commun. Phys.* **4**, 119 (2021).
55. Ge, C. et al. Modulating interlayer and intralayer excitons in WS_2/WSe_2 van der waals heterostructures. *AIP Adv*. **13**, 115101 (2023).
56. Castellanos-Gomez, A. et al. Deterministic transfer of two-dimensional materials by all-dry viscoelastic stamping. *2D Mater.* **1**, 011002 (2014).
57. Falin, A. et al. Mechanical properties of atomically thin boron nitride and the role of interlayer interactions. *Nat. Commun.* **8**, 15815 (2017).
58. Liu, K. et al. Elastic properties of chemical-vapor-deposited monolayer MoS_2, WS_2, and their bilayer heterostructures. *Nano Lett.* **14**, 5097 (2014).
59. Surendran, J. T. et al. Nanoparticle stressor-induced single-photon sources in monolayer WS_2 emitting into a narrowband visible spectral range. *2D Mater.* **11**, 031002 (2024).

Acknowledgements

We thank E. S. Kannan, S. R. Parne, A. Rastelli, and S. J. Cheng for the fruitful discussion and A. Rastelli for the data analysis software. This work was supported by the DST Nano Mission grant (DST/NM/TUE/QM-2/2019) and the matching grant from IIT Goa. I.D.P. thanks The Council of Scientific & Industrial Research (CSIR), New Delhi, for the doctoral fellowship. K.W. and T.T. acknowledge support from the JSPS KAKENHI (Grant Numbers 21H05233 and 23H02052) and World Premier International Research Center Initiative (WPI), MEXT, Japan.

Author contributions

Y.W. and S.S. carried out μ-PL and μ-Raman measurements supported by I.D.P. and J.T.S. under the supervision of S.K. S.S. fabricated the samples supported by J.T.S under the supervision of S.K. K.W. and T.T. prepared the hBN material. Y.W. and S.K. analyzed the data supported by J.T.S. and I.D.P. S.K. led the interpretation of the results. Y.W. and S.K. wrote the manuscript. All authors discussed the results and contributed to the manuscript. S.K. conceived and coordinated the project.

Competing interests

The authors declare no competing interests.

Additional information

Supplementary information The online version contains supplementary material available at https://doi.org/10.1038/s43246-025-00809-z.

Correspondence and requests for materials should be addressed to Santosh Kumar.

Peer review information *Communications Materials* thanks Elizabeth Peterson and the other, anonymous, reviewer(s) for their contribution to the peer review of this work. Primary Handling Editors: Zakaria Al Balushi and Aldo Isidori. A peer review file is available.